Chinese Chemical Letters 32 (2021) 755–760

Contents lists available at ScienceDirect

Chinese Chemical Letters

journal homepage: www.elsevier.com/locate/cclet

Communication

# A novel ball-in-ball hollow oxygen-incorporating cobalt sulfide spheres as high-efficient electrocatalyst for oxygen evolution reaction

Yurong Li[1], Qifei Guo[1], Yimin Jiang, Wei Shen, Ming Li, Rongxing He*

*College of Chemistry and Chemical Engineering, Southwest University, Chongqing 400715, China*

ARTICLE INFO

*Article history:*
Received 16 March 2020
Received in revised form 8 April 2020
Accepted 10 May 2020
Available online 13 May 2020

*Keywords:*
Oxygen doped
Sulfides
Kirkendall effect
Oxygen evolution reaction
Electrocatalyst

ABSTRACT

Transition-metal chalcogenides with hollow nanostructure, especially cobalt sulfides, are considered as the most promising non-precious metal catalysts for oxygen evolution reaction. However, it is difficult to synthesize oxygen-containing cobalt sulphides with hollow structure due to the different physical/chemical properties between metal sulfides and metal cobalts. Herein, we report a novel oxygen-containing amorphous cobalt sulfide ball-in-ball hollow spheres (Co-S-O BBHS) synthesized by an anion exchange method. Taking advantage of the ball-in-ball hollow structure, the amorphous Co-S-O BBHS shows superior oxygen evolution reaction (OER) electrocatalytic performance with a low overpotential of 285 mV at 10 mA/cm$^2$, small Tafel slope of 49.67 mV/dec, high Faraday efficiency of 96%, and satisfied durability. Experiments and DFT calculations demonstrate that the introduction of oxygen and sulfur modulates the electronic structure of Co-S-O BBHS, thus enhancing the adsorption of *O (adsorbed O species on catalyst surface) intermediate, which greatly boosts the catalytic activity towards OER. This work provides a new strategy for controllable synthesis of complex hollow structures of transition-metal chalcogenides for OER.



Electrochemical water splitting has been known as a promising and environmental approach to produce hydrogen by avoiding dependence on fossil fuels [1–3]. The efficiency of hydrogen generation depends enormously on the anodic oxygen evolution reaction (OER) [4,5]. However, due to multistep reaction involving four-electron transfer, OER has high kinetic barrier, large overpotential and low efficiency [6]. Accordingly, the development of high-performance elecrtocatalysts for OER is a crucial step for water splitting. As is known to all, Pt- and Ru-based materials are the benchmark catalysts for OER, but the resource scarcity, high cost and poor stability of Pt- and Ru-based catalysts greatly hinder their large scale application. To meet these challenges, great effort has been given to reduce the overpotential of OER kinetics using cheaper earth abundant materials as elecrtocatalysts, such as transition metal oxides/hydroxides [7,8], sulfides [9–11], nitrides [12,13], phosphides [14,15], and selenides [16]. Nevertheless, the catalytic activity of these catalysts is still not as good as that of noble metal-based catalysts.

Catalytic activity is an important indicator for evaluating the efficiency of electrocatalysts, which is controlled by the number of active sites and efficient mass transport [17]. Scientists have found that oxygen doping could enhance the activity of sites and conductivity for promoting catalytic activity [18,19]. This can be explained that the formed functional groups, such as hydroxyl one, interact with water molecules by hydrogen bonding to render them hydrophilic or act as anchoring sites to immobilize active nanoparticles. Wen and co-workers reported an oxygen-incorporated amorphous $CoS_x$ porous nanocubes as high-activity OER electrocatalysts [20]. On the other hand, to increase the amount of active sites per unit area, various amorphous materials were fabricated and used as electrocatalysts. For example, Zhen *et al.* reported that the OER catalytic activity of amorphous cobalt sulfide hollow microplates is significantly improved due to favorable hollow structural ordering and large number of active sites [21]. Among all kinds of hollow nanostructures, cobalt sulfide catalysts with multi-shell hollow spheres have received more interest due to their special properties, including large surface area, accessible active sites, and confined interior space. However, it is a great challenge to synthesize complex hollow structures of oxygen-containing cobalt sulfides because of the distinct physical/chemical properties between metal sulfides and metal oxides [1].

Motivated by the above issues, herein we successfully synthesized one kind of novel oxygen-containing amorphous cobalt sulfide ball-in-ball hollow spheres (Co-S-O BBHS) by mean of anion exchange and Kirkendall effect. At the anion exchange process, the

* Corresponding author.
*E-mail address:* herx@swu.edu.cn (R. He).
[1] These authors contributed equally to this work.

https://doi.org/10.1016/j.cclet.2020.05.012

target product not only formed the special hollow structure, but also produced a large number of defect sites. Moreover, the surface of the precursor is not compact by calcination, which is conducive to the ion exchange reaction. As we expected, the as-prepared Co-S-O BBHS composites exhibit remarkable catalytic performance for OER in 1 mol/L KOH with the overpotential of 285 mV at a current density of 10 mA/cm$^2$. The density functional theory (DFT) calculations indicate that sulfur significantly regulates the electronic structure of the amorphous Co-S-O BBHS, and the introduction of oxygen remarkably strengthens the binding energy between intermediates (*O) and active sites, which promote catalytic activity for water oxidation reaction.

The anion exchange and Kirkendall effect were utilized to form the ball-in-ball hollow spheres in this work, which is similar to that reported by Yu and co-workers [1,22]. However, the formation of Kirkendall voids and amorphous materials is more difficult because of the great difference in physical and chemical properties between bimetallic oxides and mono-metallic oxides [23]. Therefore, polyvinyl pyrrolidone (PVP) was used as a surfactant to control the morphology of the precursor and prevented well crystallization [24]. The releasing of $CO_2$ from carbonates causes defects on the surface of $Co_3O_4$ precursor and makes it is not compact, which is beneficial to ion exchange reaction [25]. Fig. S1 (Supporting information) schematically demonstrates our design notion for synthesis of the amorphous Co-S-O BBHS catalysts. In the method, cobalt nitrate, sodium bicarbonate and PVP were firstly mixed in the ethylene glycol for 20 h at 200 °C, then the product was calcined at 300 °C to prepare sea urchin-like $Co_3O_4$ precursor. After that, the precursors of sea urchin-like $Co_3O_4$ were transformed into the amorphous Co-S-O BBHS by solution sulfidation process (the experimental details were given in Supporting information). One of the key factors in the formation of ball-in-ball hollow spheres is the long-term supply of sulfide ions during thioacetamide (TAA) decomposition. Sulfur ions ($S^{2-}$) are continuously generated and the solution changes from neutral to acidic, which makes ion exchange reaction easier to occur. $S^{2-}$ chemically etches the surface of the precursor to form smooth nanoparticles and reacts with cobalt ions to produce the oxygen-containing amorphous cobalt sulfide shell on the reaction interface. When the outward diffusion of cobalt ions is faster than the inward diffusion of $S^{2-}$, Kirkendall voids are formed in the interior of the precursor, and the intermediate yolk-shell structure is produced. With the decrease of cobalt ions migration rate, the gap between the core and shell expands. When the ion exchange reaction is completed, the core forms the second shell. Finally, the unique ball-in-ball hollow spheres structure is obtained.

The morphologies and microstructures of the as-synthesized samples were identified by scanning electron microscopy (SEM), transmission electron microscopy (TEM), and high-resolution transmission electron microscopy (HRTEM). The SEM image clearly shows that the surface of the ball is uniformly covered with nano-spines, presenting a nano-structure similar to that of sea urchin (Fig. 1a). At a higher magnification, we observed that these nano-spines grow regularly on the surface of the ball (Fig. S2 in Supporting information). The corresponding TEM image (Fig. 1b) shows the precursor is solid, and the length of spines on the sphere surface is generally distributed in the ranging of 50−400 nm, as displayed in Fig. S3 (Supporting information). The HRTEM image (Fig. 1c) shows that the lattice fringes of 0.29 nm and 0.47 nm are corresponding to the (220) and (111) facets of $Co_3O_4$. However, during the formation of the ball in ball structure, the concentrations of $S^{2-}$ ions and reaction temperature have great influence on the morphology of the catalysts (Supporting information). The low temperature experiment was carried out at 120 °C for 6 h, in which the hollow structures were difficult to form due to the slow sulfidation, while at a higher temperature of 200 °C for 6 h, the hollow sphere with single shell structure was obtained after sulfidation. The results show that temperature not only affects the diffusion rate of ions, but also influences the decomposition rate of TAA. TEM images of products under different sulfidation conditions were shown in Fig. S4 (Supporting information). Therefore, the different diffusion rate of sulfur and cobalt ions caused by sulfur ion concentration and reaction temperature are of great significance for the successful synthesis of target products [26,27]. After sulfidation, the obtained amorphous Co-S-O BBHS maintains the spherical architecture, and the size is greatly reduced

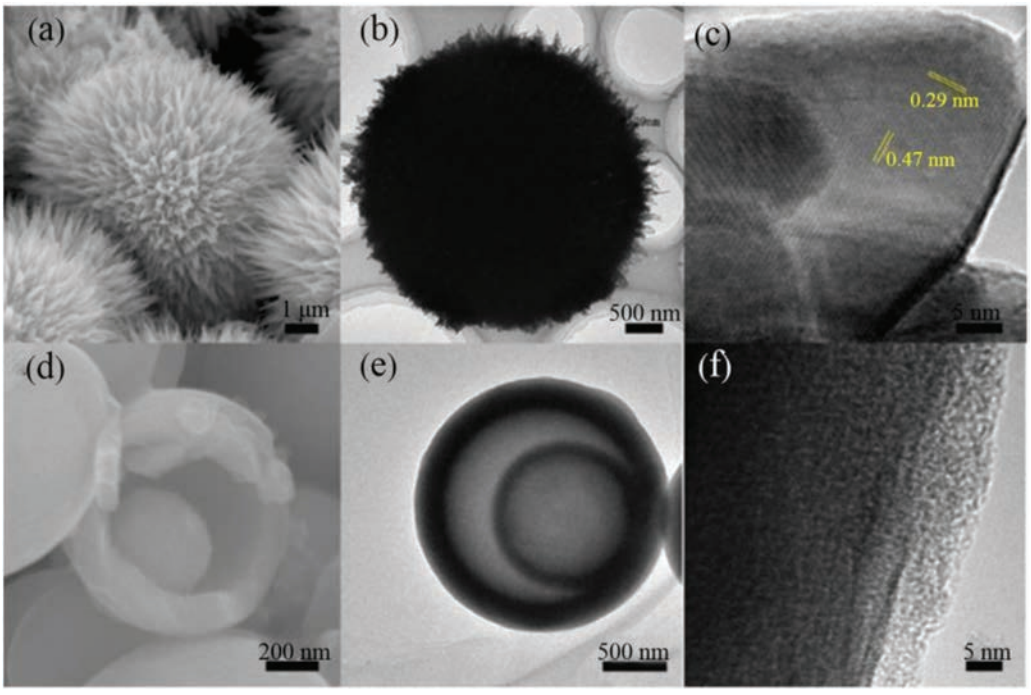


**Fig. 1.** SEM (a), TEM (b) and HRTEM (c) images of $Co_3O_4$ sea urchin. SEM (d), TEM (e) and HRTEM (f) images of amorphous Co-S-O BBHS.

compared with that of the precursor (Fig. 1d). TEM images (Fig. 1e) provide a visual way to analyze the internal structure of the spheres, by displaying notably contrast differences in transparency between hollow and solid parts. Approximately estimating from TEM images, the average diameters of the inner and outer shells are about 440 nm and 650 nm, respectively. As shown in Fig. 1f, the absence of lattice fringes proves that Co-S-O BBHS is amorphous. According to the energy dispersive spectrum (EDS) (Fig. S5 and Table S1 in Supporting information), the sample consists of Co, S and O elements with Co/S ratio of about 0.63, which verifies that the product is a nonstoichiometric compound. Fig. 2a shows the X-ray diffraction (XRD) patterns. The XRD pattern of the precursor exhibits five peaks at $2\theta = 31.2^\circ$, $36.8^\circ$, $44.8^\circ$, $59.3^\circ$ and $65.2^\circ$, which correspond to the diffractions of (220), (311), (400), (511) and (440) planes of the cubic phase $Co_3O_4$ (JCPDS No. 43-1003), respectively. For the target product, the XRD shows no obvious diffraction peaks, indicating the amorphous nature of the product, which is consistent with the HRTEM result (Fig. 1f).

In order to further analyze the chemical state and elemental composition of Co-S-O BBHS, the X-ray photoelectron spectroscopy (XPS) was performed. The XPS analyses reveal that Co-S-O BBHS include Co, S, O and C elements, which can be confirmed from the full spectrum (Fig. 2b). Note that the signal of C is attributed to the conductive adhesive carbon tape used to fix the catalyst in XPS measurement. The element atomic ratio shown in Table S2 (Supporting information) is approximately same as the EDS result. The Co 2p XPS spectrum of Co-S-O BBHS is exhibited in Fig. 2c. The two peaks at 778.4 eV and 793.5 eV can be identified as the peaks of Co-S bond. The other pair of peaks at about 781.4 eV and 797.5 eV belong to Co-O bond. Moreover, the satellite peaks at 786.8 eV and 803.0 eV are indexed to $Co^{2+}$ ions [28,29]. Fig. S6 (Supporting information) shows the O 1s XPS spectrum, in which two peaks located at 531.3 eV and 532.0 eV correspond to Co—O and O—S bonds, respectively. The peak of 532.9 eV is usually associated with defects, under-coordinated lattice oxygen [30,31]. In the S 2p spectrum (Fig. 2d), the two peaks at 161.5 eV and 162.2 eV are respectively attributed to the S $2p_{3/2}$ and S $2p_{1/2}$, belonging to Co-S bond. The peaks at 168.5 eV and 169.1 eV correspond to S—O bond because that the sulfur binds to oxygen on the surface of material [32]. The XPS analysis shows that oxygen is successfully doped into the amorphous Co-S-O BBHS.

Considering the advantage of a large number of exposed catalytic active sites, the OER catalytic activity of Co-S-O BBHS and $Co_3O_4$ were investigated by linear sweep voltammograms (LSV) in 1 mol/L KOH with the scan rate of 10 mV/s (Fig. 3a). The catalytic performance of $RuO_2$ was also plotted as reference. The overpotential of 10 mA/cm$^2$ measured according to the results of LSV [33], is often used as a benchmark to assess the activity of OER catalysts. The precursor of $Co_3O_4$ has a unique sea urchin structure, its electrocatalytic performance for OER is better than 2D nanosheet and 3D nanocube, demonstrating that the shape affects electrocatalytic performance [34]. The amorphous Co-S-O BBHS catalyst exhibits the highest electrocatalytic activity with the lowest overpotential of 285 mV to reach 10 mA/cm$^2$, which is much smaller than that of $Co_3O_4$ (320 mV) and commercial $RuO_2$ (295 mV). The low overpotential of the amorphous Co-S-O BBHS may be the regulation of electronic structure caused by the synergistic action of O and S. The potential change before and after sulfuration is also a good index to judge whether S is introduced into $Co_3O_4$ catalysts. Furthermore, the overpotential of the amorphous Co-S-O BBHS at 10 mA/cm$^2$ is much lower than that of most Co-based electrocatalysts and other state-of-art OER

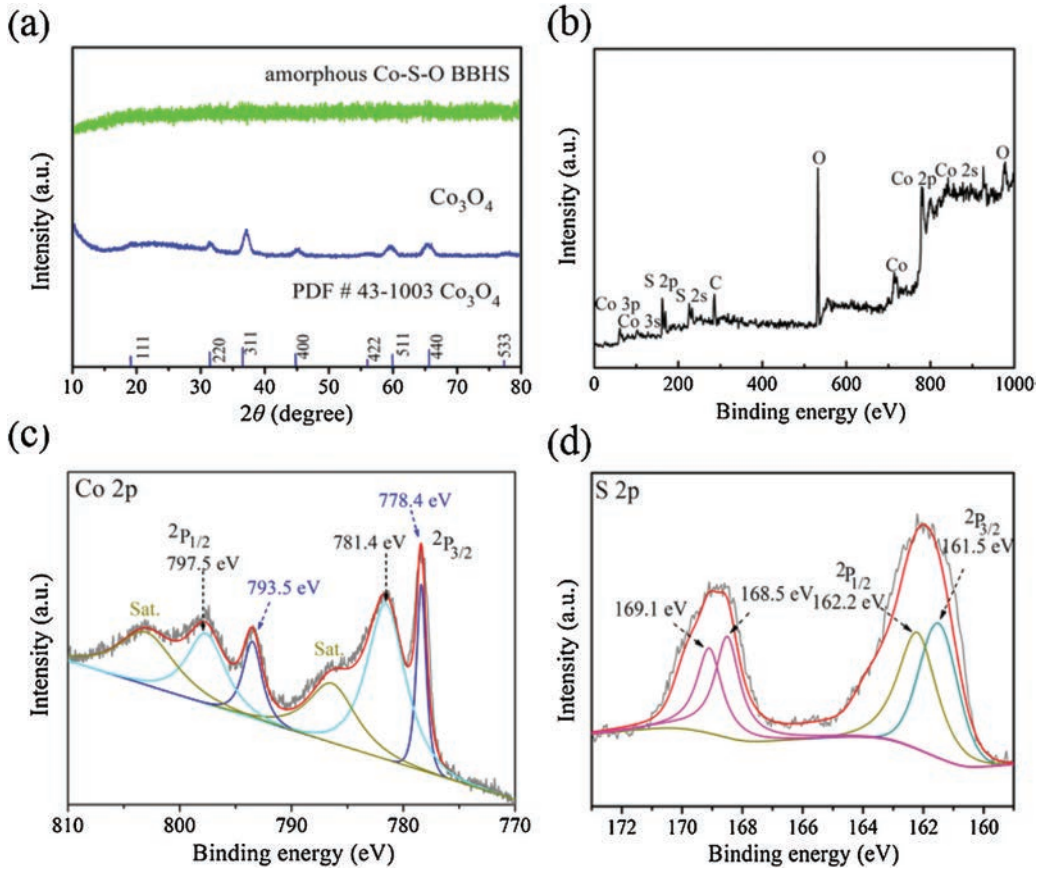


**Fig. 2.** (a) XRD patterns of amorphous Co-S-O BBHS and $Co_3O_4$ sea urchin. (b) XPS survey spectrum for amorphous Co-S-O BBHS. (c) Co 2p and (d) S 2p XPS spectrum of Co-S-O BBHS.

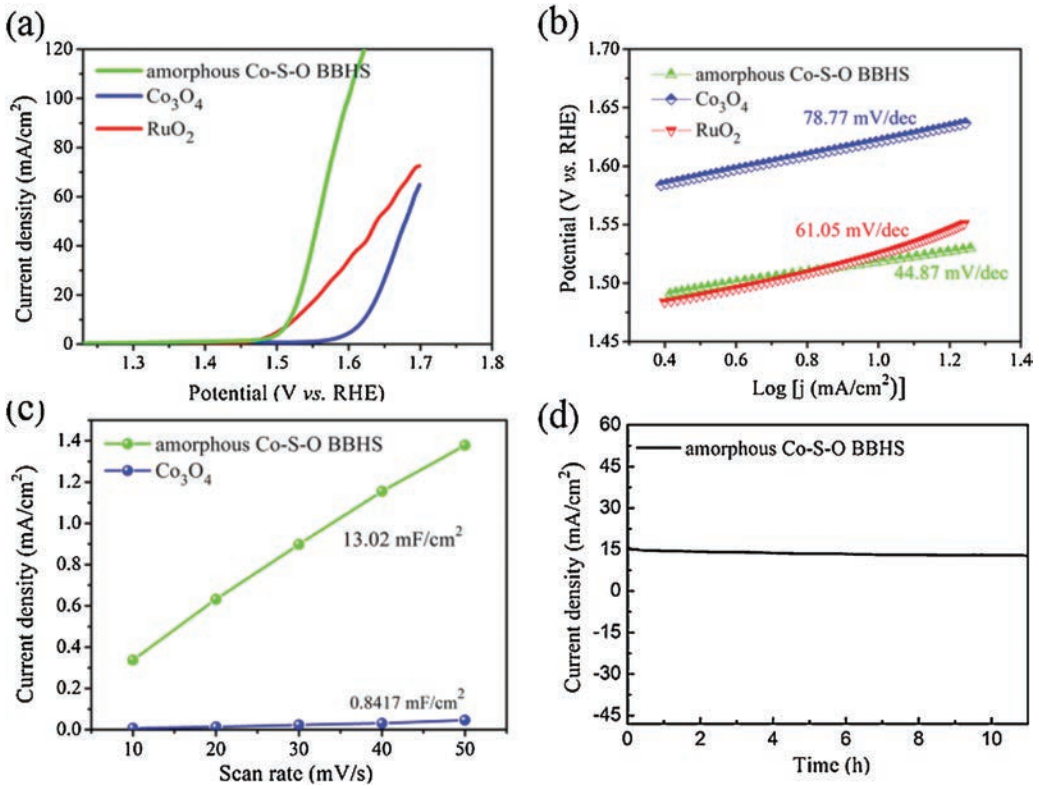


**Fig. 3.** (a) Polarization curves for OER at a scan rate of 10 mV/s in 1.0 mol/L KOH and (b) the corresponding Tafel plots. (c) Double layer capacitance ($C_{dl}$) of amorphous Co-S-O BBHS and $Co_3O_4$ sea urchin. (d) Chronoamperometric response of amorphous Co-S-O BBHS in 1.0 mol/L KOH solution.

eletrocatalysts (Table S3 in Supporting information). Tafel analysis is used to evaluate the OER kinetics of the amorphous Co-S-O BBHS and other catalysts. It is well known that the small Tafel slope indicates favorable electrochemical reaction kinetics, which may provide worthy guidance for the design of OER electrocatalyst [35]. The Tafel slope of the amorphous Co-S-O BBHS is only about 44.87 mV/dec (Fig. 3b), which is much lower than that of $Co_3O_4$ (78.77 mV/dec) and $RuO_2$ (61.05 mV/dec). The low Tafel slope of

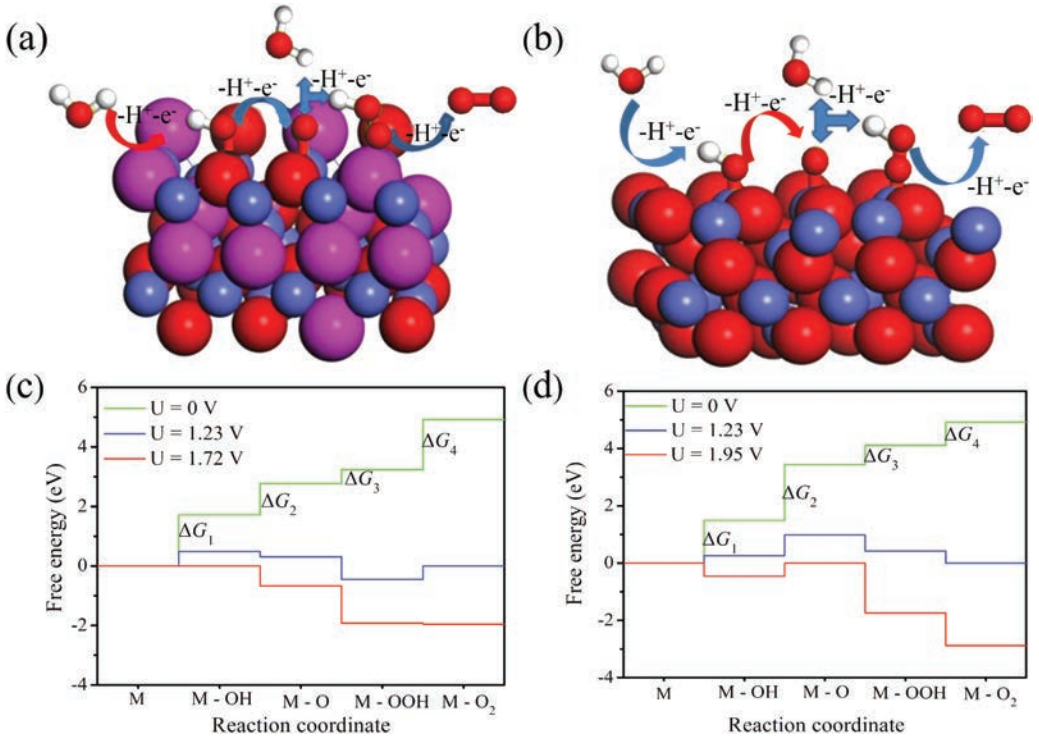


**Fig. 4.** OER process on the surface of amorphous Co-S-O BBHS (a) and $Co_3O_4$ (b). Gibbs free energy change ($\Delta G$) of the OER process on the surface of amorphous Co-S-O BBHS (c) and $Co_3O_4$ (d). Blue ball is cobalt, red represents oxygen, pink is sulfur, and white is hydrogen.

Co-S-O BBHS indicates that it has faster reaction kinetics in OER. Combined with the LSV result in Fig. 3a, one can find that the activity of Co-S-O BBHS is significantly higher than other catalysts in 1.0 mol/L KOH solution.

To further assess the OER reaction kinetics, the electrochemical impedance spectroscopy (EIS) tests were performed (Fig. S7 in Supporting information). All samples were tested in 1.0 mol/L KOH. The Nyquist plots suggest that the amorphous Co-S-O BBHS possess the smaller interfacial charge transfer resistance and faster electron transfer process than $Co_3O_4$, therefore possessing good electrical conductivity. Electrochemical surface area (ECSA) is one of the important factors affecting the performance of electrocatalysts. In order to analyze the difference of catalytic properties between the two electrode materials (Co-S-O BBHS and $Co_3O_4$), their ECSAs were compared by researching the double layer capacitance ($C_{dl}$) in non-faradic region at different scanning rates (Fig. 3c). The $C_{dl}$ was obtained from cyclic voltammetry test (Fig. S8 in Supporting information). As shown in Fig. 3c, $C_{dl}$ of the Co-S-O BBHS catalyst (13.02 m F/cm$^2$) is higher than that of $Co_3O_4$ (0.8417 mF/cm$^2$), indicating that more active sites are exposed. Indeed, the large ECSA of Co-S-O BBHS is due to its unique hollow structure and excellent conductivity, which is conducive to improving the efficiency of OER. High durability of electrocatalyst is of great significance for energy conversion systems. The stability of Co-S-O BBHS electrode was studied using chronoamperometry in alkaline solution. The tested result (Fig. 3d) suggests that the electrocatalytic activity of the Co-S-O BBHS electrode can be maintained for a long time without obvious change. In addition, to prove that the observed current density is attributed to water oxidation rather than side reactions, the Faraday efficiency is measured by rotating ring-disk electrode (RRDE) technique [36]. The Faraday efficiency testing mechanism of the RRDE was shown in Fig. S9 (Supporting information). When a constant current (300 μA) was passed through the disk electrode for $O_2$ generation, the detected ring current was about 57.5 μA (Fig. S10 in Supporting information). In this case the measured Faraday efficiency is about 96%. The high Faraday efficiency indicates that the catalytic current is completely caused by water oxidation. These results confirm that Co-S-O BBHS is a stable and highly active electrocatalyst for OER.

Obviously, the above discussion reveals that the excellent catalytic activity of the amorphous Co-S-O BBHS is mainly attributed to its superior structural characteristics and chemical compositions. The special amorphous structure of catalyst is formed by combining two hollow balls, and the hollow part of the interior can be considered as a reservoir of electrolytes, which facilitates rapid diffusion and related reactions. In addition, the significant increase of the surface area, which provides a large number of active sites for the redox reaction, leads to higher catalytic activity. Generally, amorphous materials exhibit unique physical and chemical properties, with isotropy nature and more active sites [37,38]. The amorphous Co-S-O BBHS has outstanding stability due to its isotropy. Moreover, Co-S-O BBHS can withstand large change of catalyst volume in the redox process [39]. Since amorphous shells have more ions transport channels, which not only displays excellent OER performance, but also provides enough place for the reservoir of electrolyte.

To dissect the effects of incorporated O and S on the catalytic activity, the theoretical models of Co-S-O BBHS and $Co_3O_4$ were illustrated in Figs. 4a and b and Fig. S11 (in Supporting information) and DFT calculations were performed. Previous computational studies have shown that the oxygen evolution activity is closely related to the chemisorption energy of OER intermediates [40]. In an alkaline medium, it is recognized that the overall OER process at the anode is divided into four one-electron transfer steps [41]. The process of OER can be summarized into five states: Original catalyst, catalyst-OH, catalyst-O, catalyst-OOH and catalyst-$O_2$ (Fig. 4). In the constructed models, the OER intermediates (*OH, *O and *OOH (*X denotes adsorbed X species on catalyst surface) were added on the surface of models (Figs. 4a and b). The distances between Co and intermediates (*OH, *O and *OOH) in four transfer steps were listed in Table S4 (Supporting information). For Co-S-O BBHS, the energy profile shows that the Gibbs free energy change ($\Delta G$) is the largest when the catalyst-OH state is formed. This indicates that the formation of catalyst-OH state ($OH^- + * \rightarrow *OH + e^-$) is the slowest step and thus the rate-determining step of the whole OER process. Similarly, the formation of catalyst-O state ($*OH \rightarrow *O + H^+ + e^-$) is the rate-determining step for $Co_3O_4$. The OER activity can be evaluated by directly comparing the $\Delta G$ of the rate-determining steps of these two catalysts [42]. The rate-determining step $\Delta G$ of Co-S-O BBHS is about 1.72 eV, which is smaller than that of $Co_3O_4$ (~1.95 eV), suggesting that the Co-S-O BBHS catalyst achieves higher electrocatalytic activity toward OER than $Co_3O_4$ (Table S5 in Supporting information). This can be reasonably explained that the introduction of sulfur anions regulates the electronic structure of Co-S-O BBHS and reduces energy barrier of the rate-determine step during OER. These results suggest that the electronic conductivity and electron transfer capacity of the Co-S-O BBHS catalyst increase relative to that of $Co_3O_4$, which is consistent with the results of EIS tests. The synergistic effect of oxygen and sulfur significantly greatly boosts the OER catalytic activity of the Co-S-O BBHS catalyst by increasing the adsorption of intermediates on active sites, which is confirmed by the calculated $\Delta G$ data (Table S5).

In summary, the oxygen-incorporating amorphous cobalt sulfides with unique ball-in-ball hollow structure, Co-S-O BBHS, were successfully prepared by utilizing the discrepancy in diffusion rate of cobalt cations and sulfide anions, in which a long-term and stable supply of sulfide ions during TAA decomposition is a key factor to form the Co-S-O BBHS catalyst. Systematic studies of materials characterization, electrochemical tests and DFT calculations confirmed that the amorphous Co-S-O BBHS exhibits outstanding catalytic activity and stability towards OER in alkaline medium. This is because that the ball-in-ball hollow structure of Co-S-O BBHS provides a large number of active sites and ion transport channels, and the synergistic effect of oxygen and sulfur results in the enhanced adsorption of *O intermediates on active sites. This work opens up a new way for the controllable synthesis of complex hollow structure of oxygen-containing amorphous cobalt sulfide and for the design of advanced electrocatalysts.

## Declaration of competing interest

There are no conflicts to declare.

## Acknowledgments

This work was supported by the National Natural Science Foundation of China (Nos. 91741105, 21173169), and Chongqing Municipal Natural Science Foundation (No. cstc2018jcyjAX0625).

## Appendix A. Supplementary data

Supplementary material related to this article can be found, in the online version, at doi:https://doi.org/10.1016/j.cclet.2020.05.012.

## References

[1] L. Shen, L. Yu, H.B. Wu, et al., Nat. Commun. 6 (2015) 1–8.
[2] X. Han, C. Yu, H. Huang, et al., Nano Energy 62 (2019) 136–143.
[3] M. Qu, Y. Jiang, M. Yang, et al., Appl. Catal. B: Environ. 263 (2020) 118324.
[4] F. Hu, S. Zhu, S. Chen, et al., Adv Mater. 29 (2017) 1606570–1606579.
[5] H.Y. Fang, T.Z. Huang, D. Liang, et al., J. Catal. 371 (2019) 185–195.

[6] G. Shi, C. Yu, Z. Fan, J. Li, M. Yuan, ACS Appl. Mater. Interfaces 11 (2019) 2662–2669.
[7] J. Liu, J. Nai, T. You, et al., Small 14 (2018) e1703514.
[8] S. Lei, Q. Li, Y. Kang, Z. Gu, J. Zhang, Appl. Catal. B: Environ. 245 (2019) 1–9.
[9] Y. Luo, X. Li, X. Cai, et al., ACS Nano 12 (2018) 4565–4573.
[10] D. He, X. Wu, W. Liu, et al., Chin. Chem. Lett. 30 (2019) 229–233.
[11] M. Wang, C.L. Dong, Y.C. Huang, S. Shen, ACS Catal. 10 (2020) 1855–1864.
[12] S. Dutta, A. Indra, Y. Feng, H. Han, T. Song, Appl. Catal. B: Environ. 241 (2019) 521–527.
[13] S. Zhao, M. Li, M. Han, et al., Adv. Funct. Mater. 28 (2018) 1706018.
[14] M. Qu, Y. Jiang, M. Yang, et al., Appl. Catal. B: Environ. 263 (2020) 118324.
[15] L. Jin, H. Pang, Chin. Chem. Lett. 31 (2020) 2300–2304.
[16] S. Liu, Y. Jiang, M. Yang, et al., Nanoscale 11 (2019) 7959–7966.
[17] Z.W. Seh, J. Kibsgaard, C.F. Dickens, et al., Science 355 (2017) eaad4998.
[18] S. Chen, J. Duan, M. Jaroniec, S. Qiao, Angew. Chem. 52 (2013) 13567–13570.
[19] Y. Hou, Z. Wen, S. Cui, X. Feng, J. Chen, Nano Lett. 16 (2016) 2268–2277.
[20] P. Cai, J. Huang, J. Chen, Z. Wen, Angew. Chem. 56 (2017) 4858–4861.
[21] H. Liu, F.X. Ma, C.Y. Xu, et al., ACS Appl. Mater. Interfaces 9 (2017) 11634–11641.
[22] Y.D. Yin, R.M. Rioux, C.K. Erdonmez, et al., Science 304 (2004) 711–714.
[23] H. Tianou, W. Wang, X. Yang, et al., Nat. Commun. 8 (2017) 1–9.
[24] Y. Zhang, W. Sun, X. Rui, et al., Small 11 (2015) 3694–3702.
[25] L. Hou, Y. Shi, S. Zhu, et al., J. Mater. Chem. A 5 (2017) 133–144.
[26] T. Chen, Z. Zhang, B. Cheng, et al., J. Am. Chem. Soc. 139 (2017) 12710–12715.
[27] G. Yilmaz, K.M. Yam, C. Zhang, H.J. Fan, G.W. Ho, Adv Mater. 29 (2017) 1606814.
[28] H. Zhu, J. Zhang, R. Yanzhang, et al., Adv Mater. 27 (2015) 4752–4759.
[29] S. Peng, X. Han, L. Li, et al., Small 12 (2016) 1359–1368.
[30] Y. Qi, B. Liu, L. Zhang, et al., J. Mater. Chem. A 5 (2017) 21994–22003.
[31] U.K. Sultana, T. He, A. Du, A.P. Omullane, RSC Adv. 7 (2017) 54995–55004.
[32] L.L. Feng, M.H. Fan, Y.Y. Wu, et al., J. Mater. Chem. A 4 (2016) 6860–6867.
[33] A. Wu, Y. Xie, H. Ma, et al., Nano Energy 44 (2018) 353–363.
[34] B. Sidhureddy, J.S. Dondapati, A. Chen, Chem. Commun. 55 (2019) 3626–3629.
[35] J. Zhang, L. Yu, Y. Chen, et al., Adv. Mater. 32 (2020) 1906432.
[36] S. Zhao, Y. Wang, J. Dong, et al., Nat. Energy 1 (2016) 2058–7546.
[37] Y. Jiang, Z. Dan, L. Yong, et al., Nano Energy 4 (2014) 23–30.
[38] P. Han, T. Tan, F. Wu, et al., Chin. Chem. Lett. 31 (2020) 2469–2472.
[39] Z. Han, D. Mingliang, Z. Ming, et al., Chem. Comm. 50 (2014) 15435–15438.
[40] S. Ye, Z. Shi, J. Feng, Y. Tong, G. Li, Angew. Chem. 57 (2018) 2672–2676.
[41] L.S. Peng, J. Wang, Y. Nie, et al., ACS Catal. 7 (2017) 8184–8191.
[42] M. Bajdich, M. Garciamota, A. Vojvodic, J.K. Norskov, A.T. Bell, J. Am. Chem. Soc. 135 (2013) 13521–13530.